Numerical Simulation of Ethanol−Water−NaCl Droplet Evaporation

Xingmao Jiang,[†,‡] Timothy L. Ward,[†] Frank van Swol,[§] and C. Jeffrey Brinker*[,†,§]

Department of Chemical and Nuclear Engineering and Center for Micro-Engineered Materials, The University of New Mexico, Albuquerque, New Mexico 87106, and Sandia National Laboratories, Albuquerque, New Mexico 87185

A quantitative description of droplet evaporation is important to aerosol research for nanofabrication, spray drying, fuel combustion, pollution control, and respiratory medical treatments. Evaporation is a moving-boundary problem with coupled mass and heat transport. An explicit finite-difference methodology and computer code has been developed for simulation of an evolving droplet, property data for size, and profiles for various compositions and temperature. The code accurately predicts the evaporation of pure water and pure ethanol droplets. To understand aerosol-assisted evaporation-induced self-assembly and the formation mechanism for single-crystal NaCl core/hexagonally ordered mesoporous silica shell particles, evaporation of ethanol−water−NaCl droplets in N_2 has been investigated by numerical simulation. The extended universal quasichemical (UNIQUAC) model with a Debye−Hückel term is used to describe the vapor−liquid phase equilibrium. For 1−2-μm-radius droplets with a number density of $10^7 \sim 10^8$/cm^3, it takes only tens of milliseconds to reach phase equilibrium after adiabatic or isothermal evaporation at 25 °C in the drying zone. The droplets entering a heating zone can be simply treated like a single-stage flash evaporation at 25 °C. For a 1-μm-radius droplet, after 0.18 ms of evaporation at 100 °C in N_2, the NaCl saturation ratio reaches levels as high as 1.3, first at the droplet center, where the initial NaCl nucleation and crystallization happens as a result of relatively quick evaporation and a steep gradient in the concentration of ethanol, an antisolvent for NaCl. NaCl crystallization "consumes" NaCl molecules near the droplet center and quenches the formation of new stable NaCl nuclei, favoring the formation of only one single-crystal NaCl core per droplet. The code provides guidance for the custom engineering of aerosol nanoparticle architectures.

Introduction

Aerosols have been the subject of growing importance to a broad spectrum of applications including spray drying, combustion, pollution control, microelectronics, occupational hygiene, and biomedical technology.[1−6] Material synthesis using spray and aerosol processes has been demonstrated for a wide variety of materials, including drug delivery platforms, ceramic and metallic powders, and carbonaceous materials, etc.[7−11] Spray and aerosol synthesis of particles involves solvent evaporation from precursor droplets, usually followed or accompanied by precursor reactions to produce the desired product. It has also been demonstrated that solvent evaporation can be exploited to drive the self-assembly of amphiphilic molecules within inorganic precursor solutions (evaporation-induced self-assembly or EISA), leading to oxide particles possessing templated mesoporosity with remarkable control over the pore size and mesostructural order.[12−14] The use of aerosol-asssisted EISA has also been shown to be a powerful strategy for producing particles with hierarchical porosity and multiphase composites, with a potential value as controlled release vehicles.[12−15]

The concentration gradients that develop within droplets during solvent evaporation play a critical role in the morphology of particles produced by spray and aerosol methods. The production of hollow particles in spray and aerosol processing is very well-known,[9,15,16] and the basic evaporation theory explaining the synthesis of hollow particles from simple precursor solutions has been well documented.[9,15−17] For a single precursor solution, solvent evaporation from the droplet surface leads to a higher concentration of the precursor compound at the droplet surface, with a decreasing concentration going toward the center of the droplet. In this traditional theory, the rate of solvent evaporation affects the steepness of the concentration gradients inside the droplet; solid precipitation initiates when the critical supersaturation is reached for the precursor compound.[9,15,16] On the basis of the diffusion equation modified by van der Lijn,[18] Jayanthi et al.[19] investigated the evaporation stage of solution aerosol thermolysis and simulated concentration profiles inside the droplet and proposed two criteria for solid particle formation. In a simple precursor solution, solid formation is thus predicted to initiate at the droplet surface where the precursor concentration is highest, and depending on the relative concentrations of supersaturation and saturation (solubility), hollow or nonhollow solid particle formation may occur.[9,15,16,19]

The physical picture of this process becomes considerably more complex in droplets that contain multiple solvents and/or multiple precursors. This is apparent, for example, in the recent observation of single NaCl crystals formed within the interior of mesoporous silica, produced by EISA of aerosols, where the initial nucleation apparently occurred at or near the center of an evaporating droplet.[13] Understanding the behavior of precursor systems such as the ones that contain multiple solvents and/or precursor compounds requires consideration of a rigorous thermodynamic model, coupled with multicomponent evaporation, diffusion, and energy transport models. So far, prediction of the droplet size evolution and droplet equilibrium temperature still relies on empirical correlations based on experimental data, and the correlations are available only for a limited number of solvents. We lack a detailed understanding of the temporal evolution even for pure water droplets in air. The complexity and coupled nature of such problems require numerical methods

* To whom correspondence should be addressed. E-mail: cjbrink@sandia.gov.
[†] The University of New Mexico.
[‡] Lovelace Respiratory Research Institute.
[§] Sandia National Laboratories.

10.1021/ie902042z

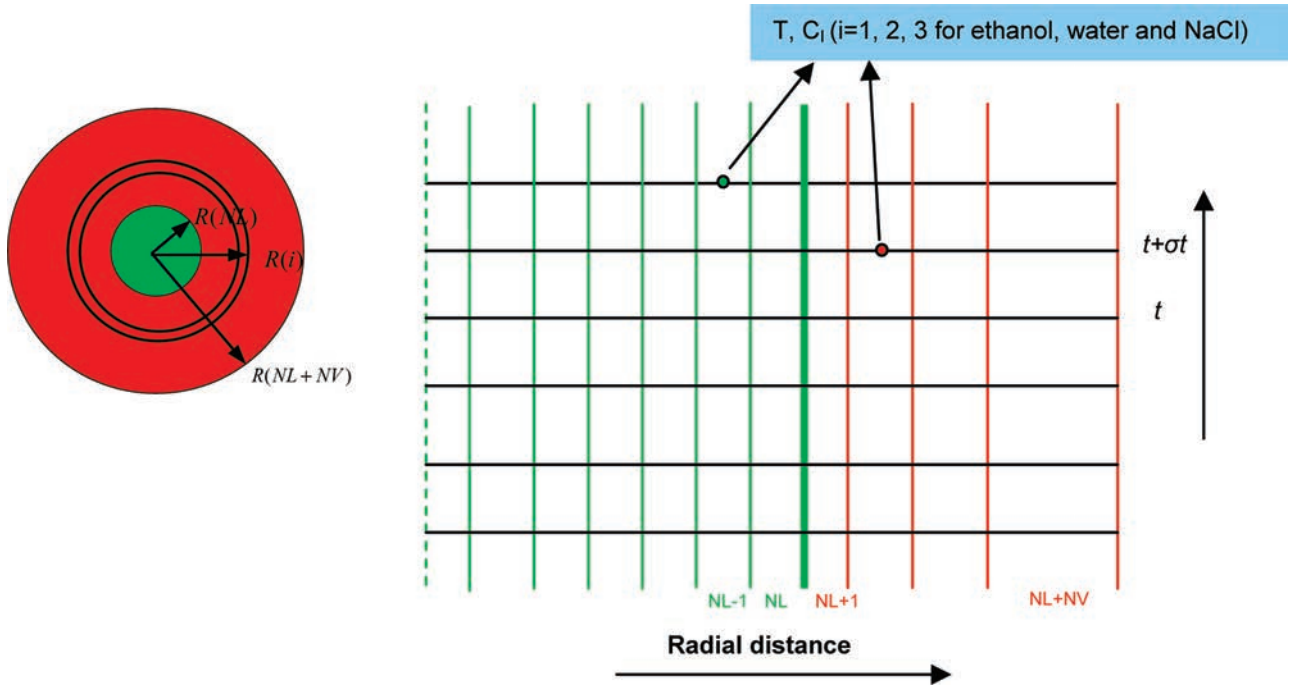

Figure 1. Scheme for a 1D evaporation grid system of droplets (green) in surrounding air (red). The liquid droplet of radius R_L is divided into NL concentric control layers. The gas phase is divided into NV concentric layers of increasing layer thickness for fast simulation.

of solution. Many methods have been tried to solve the one-dimensional (1D) time-dependent moving-boundary problem. For example, Asaithambi[20] proposed a variable time-step finite-element method. Caldwell et al.[21] provided benchmarking for the use of nodal integral and finite-difference solution of the 1D Stefan problem. The partial differential equations for the problem with implicit boundary conditions were discretized using an implicit finite-difference scheme.[22] These methods have been developed for specific problems and converge under special boundary and initial conditions.

In this paper, we have utilized a moving-boundary finite-difference method to study the evaporation of ethanol−water−NaCl droplets. We demonstrate how solvent-based solubility changes can influence the location of precipitation or solid formation, and hence the particle structure and morphology. These simulations are compared with our experimental observations for the same precursor system.

Theory and Model Development

For most evaporation phenomena, the Knudsen number, a dimensionless number defined as the ratio of the molecular mean-free path length to the droplet size, falls within the range $10^{-3}-10^{-2}$, and the evaporation system falls within the continuum regime, where the evaporation is controlled by diffusion and the coexisting phases can be assumed at equilibrium. This liquid−vapor phase equilibrium is expressed as

$$x_i P_i^s \gamma_i K_{R,i} = y_i \varphi_i^V P \tag{1}$$

where P, P_i^s, γ_i, x_i, and y_i are respectively the gas-phase total pressure and saturated vapor pressure, activity coefficient, liquid mole fraction, and vapor-phase mole fraction for component i. The vapor phase will be assumed as an ideal gas ($\varphi_i^V = 1$). $K_{R,i}$ is the Kelvin factor. For large droplets (>1 μm), the Kelvin effect can be neglected. The mass transport of an isotropic diffusion system is described by the equation of continuity for species i.

$$\frac{\partial C_i}{\partial t} = \frac{1}{r^2}\frac{\partial}{\partial r}\left(r^2 D_i \frac{\partial C_i}{\partial r}\right) \tag{2}$$

Similarly, the heat transport can be described as

$$\frac{\rho C_P}{\partial t}\frac{\partial T}{} = \frac{1}{r^2}\frac{\partial}{\partial r}\left(r^2 k \frac{\partial T}{\partial r}\right) \tag{3}$$

where t is the evaporation time, $C_i(r)$ is the local concentration of component i, T is the absolute temperature, C_P is the heat capacity at constant pressure, k is the thermal conductivity, and ρ is the mass density. Equations 2 and 3 are valid only for the evaporation without radial convection.

Approach

The above partial differential equations are difficult to solve simultaneously because all of the physical properties are interconnected and change with both time and location. To solve the moving-boundary problem, van der Lijn[18] derived the following form for a binary system using a reference-component-centered coordinate system.

$$\frac{D}{Dt}(C_i/C_r) = \frac{1}{C_r r^2}\frac{\partial}{\partial r}\left[r^2 C_r D_i \frac{\partial}{\partial r}(C_i/C_r)\right] \tag{4}$$

For a multisolvent system containing nonvolatile solutes, this is too complicated to be practical. Moreover, eq 4 still contains a substantial derivative. The validity of eq 4 relies on the assumption that there is no flux for the reference component across the moving boundary. For pure or multicomponent solvent evaporation, no such reference component exists and this method does not apply. By mathematical manipulation, one can easily derive a valid eq 5 to replace eq 2 and convert the moving-boundary problem to a conventional fixed-boundary problem. In eq 5, R is a dimensionless radius, r/R_L, and R_L is the droplet size, which is an implicit function of time.

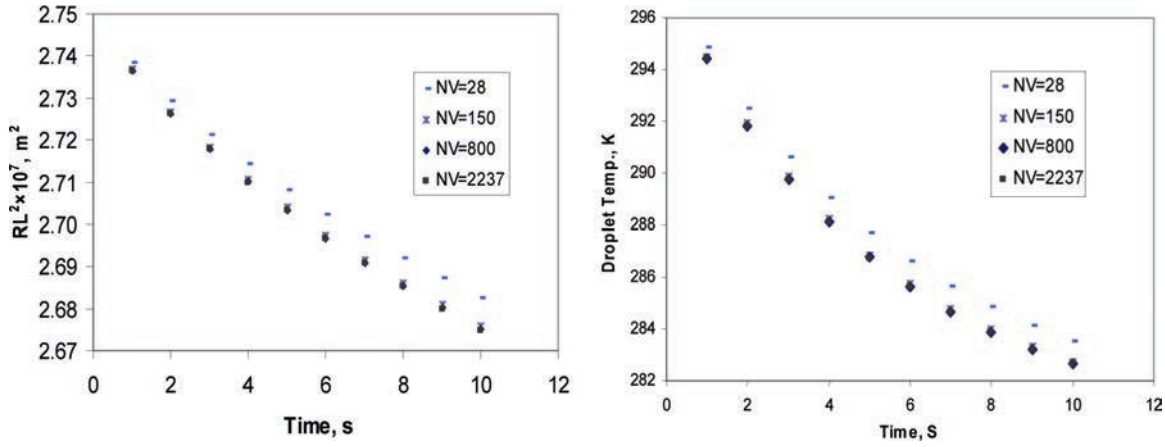

Figure 2. Predicted droplet size and average droplet temperature as a function of the evaporation time and varying vapor grid number, NV, for water droplet evaporation at atmospheric pressure.

$$R_L^2\left(\frac{\partial C_i}{\partial t}\right)\Big|_R = \frac{1}{R^2}\frac{\partial}{\partial R}\left(D_i R^2 \frac{\partial C_i}{\partial R}\right) \tag{5}$$

Although this equation is quite suitable for numerical simulation and no substantial derivative is present, it is problematic that one assumes that the multicomponent droplet keeps the same shrinkage ratio everywhere and that each element keeps a fixed dimensionless radius during evaporation. For the evaporation of droplets of initial radius $R_{L,0}$ in a still N_2 volume of equivalent radius $R_{V,0}$ determined by the aerosol droplet number density, the initial and boundary conditions for component i and details of the numerical treatment have been published previously,[14,23] but highlights are reviewed here for completeness.

As shown in Figure 1, both the droplet and surrounding gas phase are divided into a large number of concentric control shells. For fast numerical simulation, the liquid phase is divided into N_L concentric uniform or nonuniform control elements and the vapor phase of size R_V ($R_V \rightarrow \infty$ for infinite air) is separated into N_V concentric control elements.

Equations 2 and 3 are solved by a finite-difference method. Considering a uniform initial concentration distribution, the initial and boundary conditions for component i are given as follows:

$$C_i(r,0) = C_{i,0} \quad \text{for } 0 \le r \le R_{L,0} \tag{6}$$

$$C_i(r,0) = C_{i,0,V} \quad \text{for } R_{L,0} < r \le R_{V,0} \tag{7}$$

$$\left(\frac{\partial C_i}{\partial r}\right)\Big|_{r=0} = 0 \tag{8}$$

$$\left(\frac{\partial C_i}{\partial r}\right)\Big|_{R_V} = 0 \quad \text{or} \quad C_i = C_{i,\infty} \quad \text{at } R = \infty \tag{9}$$

R_L and R_V are the droplet radius and the radius of the outermost vapor layer. A subscript of 0 denotes the initial state. Similarly, the initial and boundary conditions for heat transport can be defined as

$$T(r,0) = T_{0,L} \quad \text{for } 0 \le r \le R_{L,0} \tag{10}$$

$$T(r,0) = T_{0,V} \quad \text{for } R_{L,0} < r \le R_{V,0} \tag{11}$$

$$\left(\frac{\partial T}{\partial r}\right)\Big|_{r=0} = 0 \tag{12}$$

$$\left(\frac{\partial T}{\partial r}\right)\Big|_{R_V} = 0 \quad \text{or} \quad T\Big|_{r=\infty} = T_\infty \tag{13}$$

The mass balance for component i in the liquid layer (NL) at the interface during the time interval between t and $t + \delta t$ can be written as

$$R_{NL-1}^2(R_{NL} - R_{NL-1})\frac{C_{i,NL}(t+\delta t) - C_{i,NL}(t)}{\delta t} = 2R_{NL}^2 D_{i,NL}^V \frac{C_{i,NL+1}(t) - C_{i,NL,eq}(t)}{R_{NL+1} - R_{NL}} - R_{NL-1}^2 D_{i,NL-1}\frac{C_{i,NL}(t) - C_{i,NL-1}(t)}{R_{NL} - R_{NL-1}} \tag{14}$$

For the first vapor element

$$R_{NL}^2(R_{NL+1} - R_{NL})\frac{C_{i,NL+1}(t+\delta t) - C_{i,NL+1}(t)}{\delta t} = R_{NL+1}^2 D_{i,NL+1}\frac{C_{i,NL+2}(t) - C_{i,NL+1}(t)}{R_{NL+2} - R_{NL+1}} - 2R_{NL}^2 D_{i,NL}^V \frac{C_{i,NL+1}(t) - C_{i,NL,eq}(t)}{R_{NL+1} - R_{NL}} \tag{15}$$

Similarly, the energy balance for the liquid layer (NL) can be written as the following equation:

$$RNL - 12(R_{NL} - R_{NL-1})\rho_{NL} Cp_{NL}\frac{T_{NL}(t+\delta t) - T_{NL}(t)}{\delta t} = 2R_{NL}^2 k_{NL}^V \frac{T_{NL+1}(t) - T_{NL}(t)}{R_{NL+1} - R_{NL}} + 2R_{NL}^2 \sum_i D_{i,NL}^V \frac{C_{i,NL+1}(t) - C_{i,NL,eq}(t)}{R_{NL+1} - R_{NL}}\bar{\Delta H}_{i,evp} - R_{NL-1}^2 k_{NL-1}\frac{T_{NL}(t) - T_{NL-1}(t)}{R_{NL} - R_{NL-1}} \tag{16}$$

For the first vapor element

$$R_{NL}^2(R_{NL+1} - R_{NL})\rho_{NL+1}Cp_{NL+1}\frac{T_{NL+1}(t+\delta t) - T_{NL+1}(t)}{\delta t} = R_{NL+1}^2 k_{NL+1}\frac{T_{NL+2}(t) - T_{NL+1}(t)}{R_{NL+2} - R_{NL+1}} - 2R_{NL}^2 k_{NL}^V \frac{T_{NL+1}(t) - T_{NL}(t)}{R_{NL+1} - R_{NL}} \quad (17)$$

where k is the heat conduction coefficient and $\Delta\bar{H}_i$ is the partial molar evaporation heat for component i. The solubility of air or nitrogen in the droplet is neglected. Equations 14−16 assume thermodynamic equilibrium at the liquid−vapor interface, but diffusive transport on both sides of that interface is accounted for.

Adjustment of the control volume following the updated temperature and concentration determination is achieved by self-attuning based on mass balance and pressure conservation.[14] The volume shrinkage/expansion coefficient, η_j^L, for liquid layer j over time δt can be obtained by

$$\eta_j^L = \frac{V_j'}{V_j} = \frac{\frac{4}{3}\pi(R_j'^3 - R_{j-1}'^3)}{\frac{4}{3}\pi(R_j^3 - R_{j-1}^3)} = \frac{\sum_i mw_i C_i'}{\sum_i mw_i C_i}\frac{\rho}{\rho'} \quad (18)$$

Similarly, the volume shrinkage/expansion coefficient, η_j^V, for vapor layer j over time δt is given by

$$\eta_j^V = \frac{V_j'}{V_j} = \frac{\sum_i mw_i C_i'}{\sum_i mw_i C_i}\frac{\bar{mw}}{\bar{mw}'}\frac{T'}{T} \quad (19)$$

where ρ and C are functions of the composition and temperature and mw_i is the molecular weight for component i. Primed and unprimed quantities refer to the properties after or before the time increment, respectively. The volume updating starts first from the element at the droplet center and gradually extends to the outer liquid layer and then to vapor layers while keeping a fixed total gas pressure. The initial conditions are used to update C and T and, therefore, all other transient thermodynamic and transport properties by mass balance (eq 2) and thermal balance (eq 3) for each layer over a time period $t = 0 \rightarrow \delta t$. The boundary conditions are coupled to the updating of the properties for the liquid layer at the droplet center and at the outermost vapor layer throughout the complete simulation. Step by step, all thermodynamic and transport properties for each element can be calculated over the entire evaporation time. The moving-boundary problem is solved explicitly as integration of a series of consecutive fixed-boundary heat transport only, mass transport only, and control volume shrinkage/expansion only steps. The heat transport only and mass transport only problems are solved in the same manner as that for conventional fixed-boundary problems.[14] Only if the grid sizes and time steps are small enough, the treatment should accurately simulate the actual evaporation process.

To save computation, the initial grids are designed with variable size so that the grids are dense near the droplet interface where the gradients are steep. During evaporation, the outer liquid layer (NL) shrinks and finally disappears, while the first vapor layer keeps growing bigger. The decreasing thickness for the liquid layer (NL) requires a much reduced time step, which is proportional to the square of the thickness to avoid oscillations and divergences, resulting in long computing times. The NLth liquid layer needs to be merged with the neighboring (NL − 1)th layer to save computational time. Correspondingly, the growing vapor layer (NL + 1) needs to be divided to enable quick and stable simulation and preserve the accuracy of the finite-difference method.[14] Therefore, a decreasing NL and increasing NV are expected for the moving-boundary problem. The time step can be fixed at a low value or gradually increased with developing temperature and concentration profiles to reduce computational time while ensuring convergence of the simulation.[14]

Valid correlations of the vapor−liquid equilibrium at the interface and accurate correlations for all of the thermodynamic and transport properties are required for reliable simulation. The physical properties for ethanol, water, nitrogen, and air, such as density, heat capacity, viscosity, surface tension, vapor pressure, diffusion coefficient, thermal conductivity, and enthalpy of evaporation, are correlated by polynomial regression of literature data and detailed before.[14] The extended universal quasichemical (UNIQUAC) model accurately predicts and correlates well experimental phase equilibrium diagrams for the saturated or unsaturated ethanol−water−NaCl system.[24−27] When the NaCl concentration is low, the surface tension, thermal conductivity, viscosity, and evaporation heat for the ethanol−water−NaCl liquid phase are correlated approximately the same as those for the ethanol−water solution described before.[14,23] The NaCl solubility, heat capacity, density, and component diffusion coefficients for the ethanol−water−NaCl solution are described in the Appendix.

Results and Discussion

The code has been validated with evaporation of the water droplet and ethanol droplet. Various parameters have been checked to ensure a fast, convergent, and accurate simulation.

Water Droplet Evaporation. The droplet is divided uniformly into a sufficiently large number of grids of a size of δR_L to simulate evaporation of a 1048.8-μm-diameter water droplet in still air at atmospheric pressure. A value of 100 for NL is good for fast simulation and accurate description of the droplet temperature inhomogeneity.[14]

a. Vapor-Phase Grid Distribution. The code was used to simulate water droplet evaporation in air at atmospheric pressure over 10 s to check the vapor-phase grid distribution effect. For simulation of droplet evaporation in infinite air, to save computation time, the vapor-phase grid size, R_j^V for the jth vapor layer, is designed in the power relationship given below.

$$R_j^V = R_L + (i - NL)^{1+[(j-NL-1)/NV]Q}\,\delta R_V \quad (20)$$

where R_L is the droplet size and δR_V is the initial first vapor layer thickness. The adjustable factor, Q, is selected to reduce the NV and save computation time without compromising the accuracy much. The vapor-phase size is fixed, and $R_{V,0}/R_{L,0}$ is set as high as 1132 to simulate the 10 s evaporation in an infinite vapor phase. Four different Q values have been checked, 2, 1, 0.5, and 0.1, corresponding to 28, 150, 800, and 2237 vapor layers. Fewer grids make the computation faster at the price of accuracy. Too many grids require longer computation time. As shown in Figure 2, a value of 800 for NV ($Q = 0.5$) enables convergence and accuracy for the droplet size and surface temperature.

b. Vapor Grid Size Effect. To check the vapor grid size effect, five different $\delta R_V/\delta R_L$ ratios, i.e., 0.5, 1, 2, 5, and 10, have been considered (NV = 800). All of the grid sizes have to be small enough to reduce the error for the finite-difference method. However, too small a grid spacing requires small time

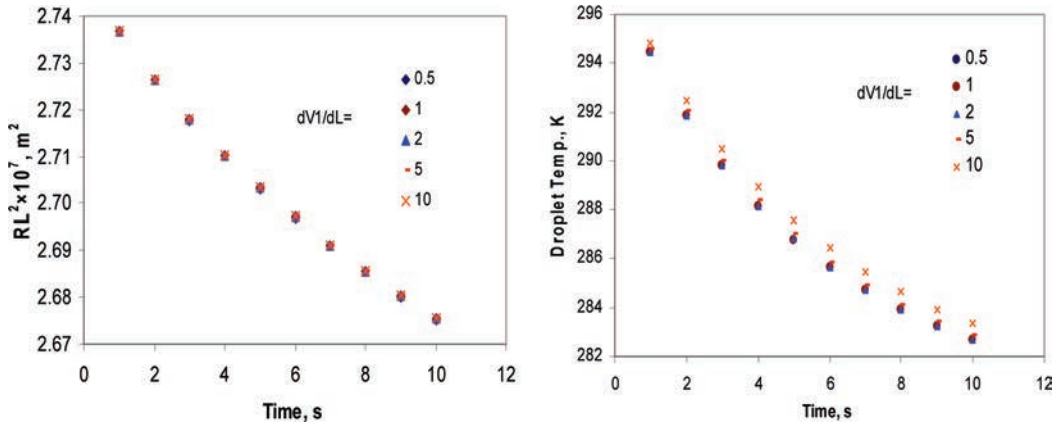

Figure 3. Predicted droplet size and droplet temperature as a function of the evaporation time and different $\delta R_V/\delta R_L$.

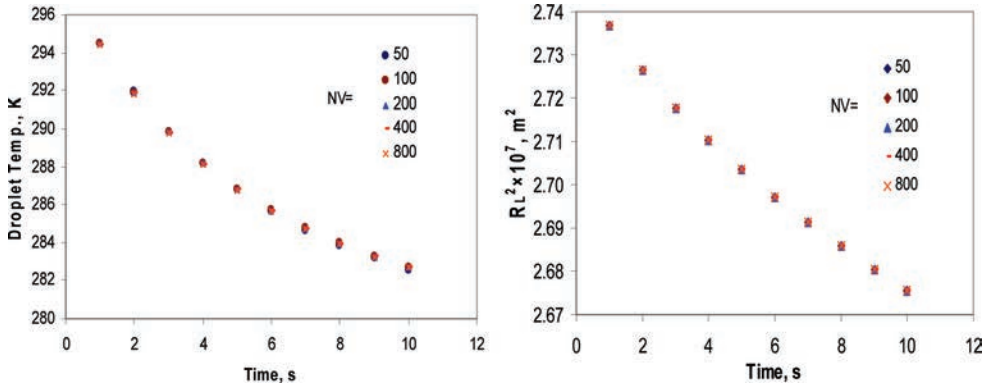

Figure 4. Predicted droplet temperature and size depletion as a function of NV and the evaporation time.

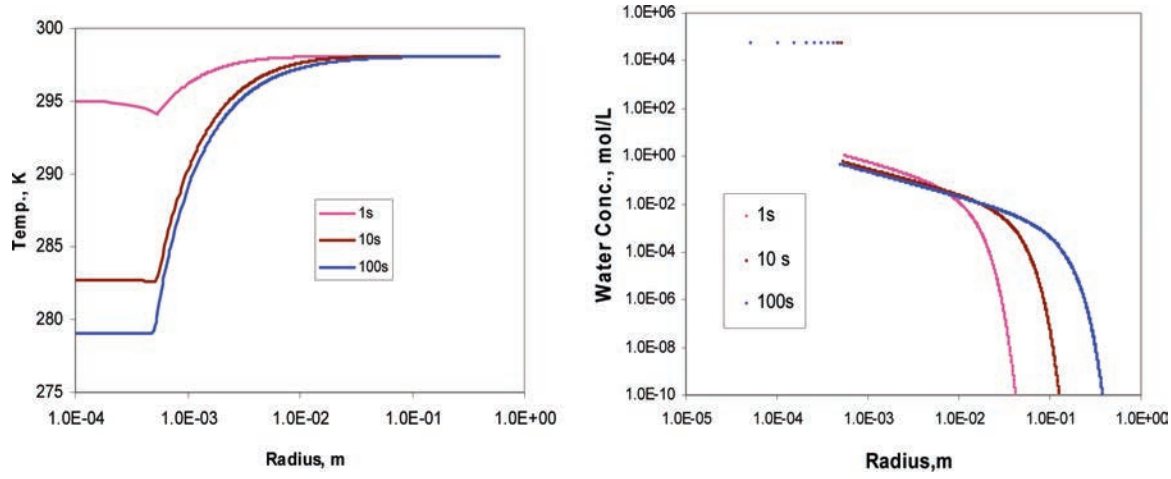

Figure 5. Temperature and water concentration profiles after 1, 10, and 100 s of evaporation.

steps and long computation time. As shown in Figure 3, selection of a big grid size will underestimate the temperature depression at the droplet surface. A ratio of 0.5 is sufficient and allows convergence.

c. Vapor Domain Size Effect. The tiny concentration gradient far away from the droplet interface makes it possible to truncate the radius at a certain value without affecting the accuracy for evaporation in infinite still air. $\delta R_V/\delta R_L$ is fixed at 0.5, Q is set as 0.5, and five different values for NV, i.e., 50, 100, 200, 400, and 800, are compared. It is found that for 10 s evaporation a value of 100 for NV is sufficient for convergence. A large value of NV is needed for longer evaporation times to maintain the accuracy.

d. Time Step Effect. A small time step has to be selected based on the grid sizes for convergence and accuracy. However, the smaller the time step, the longer the computing time. The code has been run to simulate 10 s of evaporation with different time steps, i.e., 1×10^{-6}, 1×10^{-5}, 2×10^{-5}, 4×10^{-5}, and 1×10^{-4} s. It is found that a time step of 2×10^{-5} s is close to optimal.

e. Evolution of the Temperature, Droplet Size, and Concentration during Evaporation. Figure 5 shows the temperature and water concentration profiles inside the droplet and surrounding vapor phase after 1, 10 and 100 s of evaporation. The temperatures for the droplet and surrounding vapor decrease with time. After 100 s of evaporation, the temperature

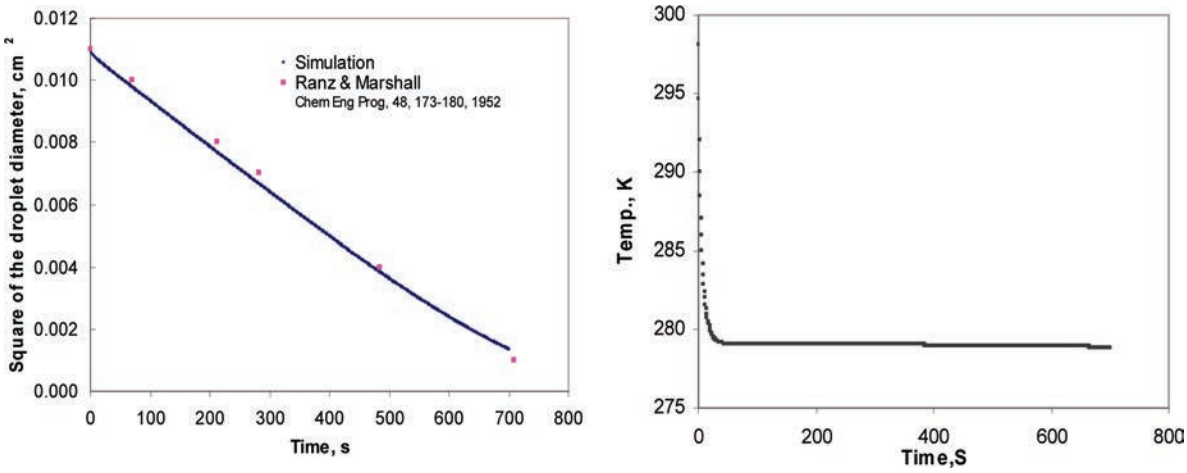

Figure 6. Predicted droplet size and mass average droplet temperature as a function of the evaporation time. Experimental data are from Ranz and Marshall.[28]

is uniform in the droplet because of high water thermal conductivity compared to mass diffusivity. During evaporation, water diffusion continuously increases the vapor-phase water concentration. After 100 s, the water concentration at the vapor-phase boundary is 10^{25} times lower than that in the droplet. The selection of a large limited vapor-phase size for numerical simulation of droplet evaporation in infinite air is thus reasonable.

Water droplet evaporation has been simulated for 700 s. As shown in Figure 6, the droplet size decreases with time and it agrees well with experimental data. Theoretically, once the temperature and concentration fields reach steady state, the square of the droplet diameter decreases linearly with time.[29] However, our simulation shows that the gradient of the square of the droplet size with respect to time is not constant. The slope decreases with time because the vapor-phase water concentration profile still develops even though the temperature field becomes stable at later times. As shown in Figure 6, the average droplet temperature decreases quickly for the first 20 s and stabilizes close to 279 K. During later evaporation, the temperature depletion slightly continues because the vapor-phase temperature profile is still relaxing as water is continuously evaporated. Sazhin[30] also observed similar phenomena and found that modeling transient droplet heating using steady-state correlations for the convective heat-transfer coefficient can be misleading. At the initial stage of heating of stationary droplets, the well-known steady-state result that the Nusselt number (*Nu*), the ratio of actual heat transfer to conductive heat transfer, equals 2 leads to underprediction of the rate of heating, while at the final stage, the same result leads to overprediction.[30]

The temperature depletion can be calculated by the following empirical equation[29] for an evaporating water droplet at a saturation ratio, S_R, of 0−5 and an ambient temperature of 273.15−313 K and at 1 atm.

$$T_d - T_\infty = \frac{(6.65 + 0.345T_\infty + 0.0031T_\infty^2)(S_R - 1)}{1 + (0.082 + 0.00782T_\infty)S_R} \quad (21)$$

For a water droplet evaporating in 24.9 °C dry air, the calculated temperature at the droplet surface according to eq 21 is 280.9 K. Our simulation predicts that the droplet temperature at equilibrium is 279 K, close to the experimental value of 282.2 K.[28] So far, there is no explicit analytical solution available in the literature that can accurately predict the equilibration time and describe the temperature evolution for these time-dependent moving-boundary problems. The code we developed can be used to predict the temperature depletion and droplet size for various solvent droplets over wide ranges for the saturation ratio, temperature, and gas pressure.

Ethanol Droplet Evaporation. Devarakonda and Ray[31,32] investigated transient evaporation of linear streams of highly monodisperse alcohol over short evaporation times. To compare with their experimental data and verify our code, we simulated evaporation of an initially 11.02 μm ethanol droplet in dry air over 0.6 ms.

The ethanol concentration profile in the vapor phase is far from linear in a double-logarithmic plot, indicating that steady-state or quasi-steady-state treatment is not appropriate. The ethanol concentration at the vapor boundary is as low as 10^{-62} mol/L. So, the selection of a large vapor domain instead of an infinite one incurs insignificant error. Unlike evaporation of a droplet in infinite still air, the ethanol droplets move down the chamber at ~10 m/s. The Sherwood number defined as $Sh = 2K_cR_P/D$ is ~4.2 instead of 2 for static evaporation, and the Nusselt number is also increased to 3.9 instead of 2.[32] The mass and heat transport by convection should have increased the evaporation rate and reduced the droplet temperature. However, interaction of the droplets in the linear streams reduced evaporation. The interaction parameter, η_{int}, is defined as the relative transfer rate of the droplet in an array to that of an isolated droplet of identical size and composition under identical environmental conditions. Sangiovanni and Labowsky[33] found that the interaction parameter for a given geometry is independent of the physical properties of the droplets. The interaction parameters for both heat and mass transport are almost the same, i.e., $\eta_{int} = \eta_m = \eta_h$. Devarakonda and Ray[31] obtained a quadratic relationship as follows:

$$\eta_{int} = 0.0611 + 0.0505\left(\frac{l}{R_P}\right) + 0.0029\left(\frac{l}{R_P}\right)^2 \quad \text{for } 3 \le \frac{l}{R_P} \le 6 \quad (22)$$

where l is the separation distance between neighboring droplets and R_P is the droplet radius. For evaporation, the experimental dimensionless separation distance l/R_P was 3.5 and the interaction parameter had been determined as 0.27. The change of the droplet size with evaporation time t can be described by the relationship[32]

$$\frac{dR_P^2}{dt} = \frac{Sh\eta_m MW_s P^s}{RT_S\rho_L} \quad (23)$$

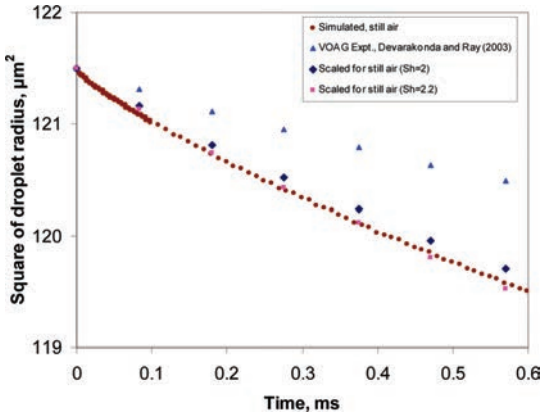

Figure 7. Predicted droplet size change versus residence time for ethanol droplets. The square of the droplet size decreases with the evaporation time. VOAG experimental data[32] are rescaled for comparison with the simulation results for still air ($Sh = 2$ and 2.2).

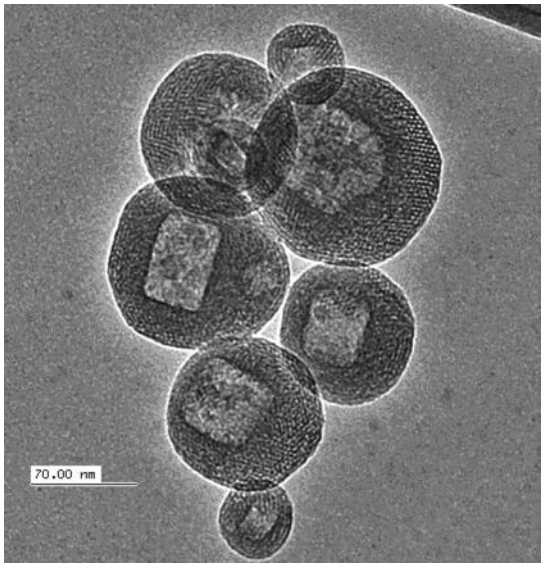

Figure 8. Transmission electron microscopy (TEM) image for single NaCl crystal/mesoporous silica core−shell particles.

where T_s is the droplet temperature at the surface, P^s is the saturated vapor pressure, and MW_s is the molecular weight. As shown in Figure 7, the experimental data of the square of the droplet size for a vibrating-orifice aerosol generator linear array droplet are rescaled by a factor of $2/Sh\eta_m$ according to eq 23, assuming a Sherwood number of 2 for an isolated static evaporating ethanol droplet. Because of the inhomogeneities of temperature, the experimental value obtained for the Nusselt number at a Reynolds number of zero was 2.23 instead of 2 for evaporating water (Ranz and Marshall).[28] Figure 7 also shows the rescaled evaporation data for static evaporation with a Sherwood number of 2.2. The simulation agrees well with experimental data for ethanol droplet evaporation.

Considering the large number of physical parameters involved in the simulation, the simulation results for both water and ethanol droplet evaporation are quite satisfactory. The general code can be used for engineering simulations of pure/multicomponent droplet evaporation under various conditions.

Ethanol−Water−NaCl Droplet Evaporation. For the EISA and formation of single NaCl crystal/mesoporous silica core−shell particles[13] (Figure 8), the polydisperse droplets generated by atomization have a mean number diameter of ~1.5 μm. The droplet number concentration is $\sim 10^7-10^8/cm^3$. The droplets were carried by nitrogen gas through a room-temperature drying zone and then a three-zone tubular furnace kept at 400 °C.

Evaporation in the Drying Zone. For droplets evaporating in ~40 cm long drying zone, the concentrations for ethanol and water and the temperatures in the vapor phase and droplets change as a result of the heat and mass transport between the droplets and surrounding air. The actual evaporation condition falls between two extremes: isothermal and adiabatic evaporation.

Isothermal Evaporation. Considering fast heat transport between the aerosol droplets with room-temperature glass tubing in the drying zone, the temperature at the vapor-phase boundary can be assumed constant at 298.15 K. For an initial 25 °C, 1 μm aerosol droplet with a NaCl mass percentage of 0.01, and a droplet number density of $8 \times 10^7/cm^3$, i.e., the radius ratio R_V/R_L ratio is ~15 and the initial ethanol concentration is set as 70% (v/v), the evaporation is very fast. As shown in Figure 9, the droplet surface temperature decreases quickly at the beginning to 292.6 K and then rebounds to 298.15 K. After ~0.01 s of evaporation, the vapor phase is at equilibrium with the liquid phase. No further change with the droplet size, temperature, and concentration occurs. The concentration, NaCl saturation ratio, and temperature are uniform within the droplet or in the vapor phase. The final saturation ratio is 0.178.

Adiabatic Evaporation. As a comparison, adiabatic evaporation of 1-μm-radius aerosol droplets in a nitrogen layer of 30 μm radius; i.e., a droplet concentration of $10^7/cm^3$ has been simulated for aerosol droplets with an initial system temperature of 25 °C and an ethanol concentration of 70% (v/v). The initial NaCl mass fraction is set at 0.02. Figure 10 shows evolution of the droplet size and surface temperature with the evaporation time separately. After ~0.028 s of evaporation, the system reaches equilibrium. The concentrations are homogeneous in both the liquid droplet and the vapor phase. The temperature is uniform, 275 K in both liquid and vapor phases. After adiabatic evaporation, the NaCl mass fraction is ~0.077 45 in the droplets.

For evaporation of the droplets of 2 μm radius, if the initial concentration, temperature, R_V/R_L ratio, and initial NaCl mass fraction are kept the same as those for the adiabatic evaporation of 1 μm droplets, the equilibrium time is increased from ~28 to ~100 ms. The final temperature, droplet size, and NaCl mass fraction are exactly the same as those for a 1 μm droplet.

Ethanol Concentration Effect. To check the effect of the ethanol concentration on evaporation, the initial ethanol concentration is increased to 80% (v/v) for the droplets of a radius of 2 μm with the same R_V/R_L ratio, temperature, and NaCl mass fraction as that for evaporation with 70% (v/v) droplets. The final temperature is 274.2 K and the equilibration time ~0.11 s, as shown in Figure 11. Compared to evaporation of 2-μm-radius, 70% (v/v) droplets, increasing the initial ethanol concentration increases the reduction in the droplet temperature and droplet size. The final NaCl mass percentage at equilibrium increases from 0.077 45 to 0.108 as a result of increased solvent evaporation.

Evaporation in the drying zone is a very fast process. A relatively long residence time of ~2 s allows sufficient time for heat transfer between the droplets and the carrier gas. We conclude that at the time that the droplets enter the heating zone the temperature can be assumed to be at room temperature and the vapor phase is at equilibrium with the liquid phase. The temperature and concentration are uniform in both the vapor and liquid phases; i.e., the vapor phase and droplets can be treated as at equilibrium after single-stage flash evaporation at 25 °C.

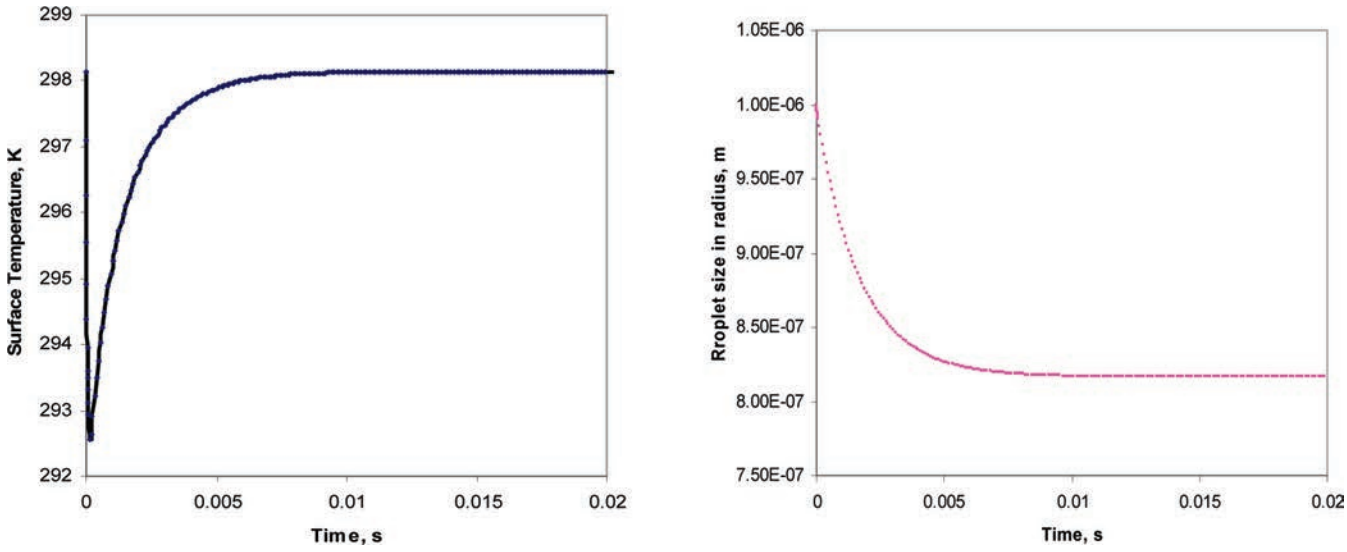

Figure 9. Droplet surface temperature change versus isothermal evaporation time (left). Droplet size change versus isothermal evaporation time (right).

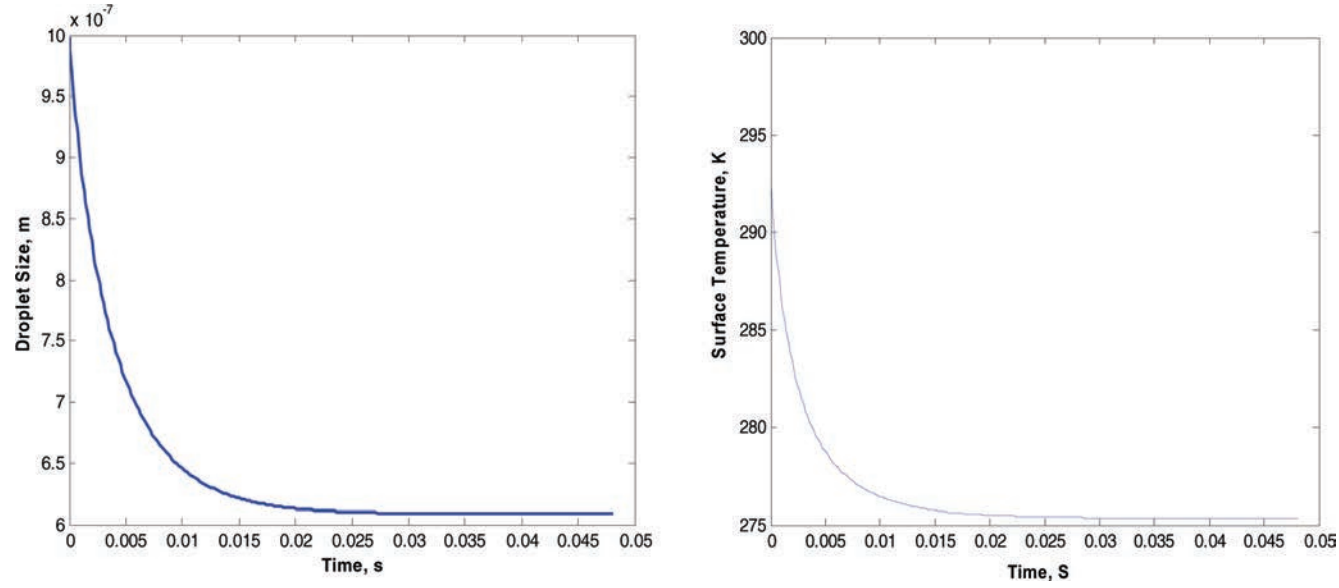

Figure 10. Droplet size change versus adiabatic evaporation time (left). Droplet surface temperature change versus adiabatic evaporation time (right).

Evaporation in the Heating Zone. In the heating zone, the temperature increases gradually from room temperature to 400 °C. The evaporation process can be assumed to consist of consecutive evaporation at increasing temperature over varying residence time. To illustrate the effect of evaporation on nucleation and crystallization, we simplify the problem and select 100 °C as the heating temperature. Evaporation in the heating zone is simulated for ethanol−water−NaCl droplets of an initial temperature of 25 °C and a droplet radius of 1 μm. The radius ratio of the vapor phase to the liquid phase (R_V/R_L) is set at 30, and the NaCl mass fraction is set at 0.08. The ethanol concentration is set at 60% (v/v). The vapor phase is in equilibrium with the droplet; i.e., the partial pressure is 0.0483 atm for ethanol and 0.0267 atm for water. The total pressure is 1 atm, with N_2 as the balance. It is assumed that NaCl nucleation and crystallization follow a homogeneous nucleation mechanism. The first nucleation and crystallization happen at the location where the saturation ratio exceeds a critical saturation ratio (a representative value of 1.3 was selected). Following ~0.183 ms of evaporation, the NaCl concentration becomes supersaturated with a maximum saturation ratio of 1.3 at the center. The temperature distribution is shown in Figure 12. The mole fraction distributions for ethanol, water, NaCl, and N_2 are shown in Figure 13. With evaporation, the concentrations for water and NaCl are enriched at the surface. The temperature profile in the liquid phase is uniform because of the large value of the Lewis number (*Le*), which is a dimensionless number defined as the ratio of thermal diffusivity to mass diffusivity. After 0.183 ms of evaporation, crystallization starts at the droplet center, and NaCl is assumed to be saturated at the center. The heat of crystallization is neglected because the heat of evaporation is much larger than the heat of crystallization and the thermal diffusivity is much higher than the mass diffusivity in the liquid phase. Quick thermal conduction makes the temperature quite uniform within the droplets during crystallization.

As shown in Figure 14, even though solvent evaporation induces enrichment of NaCl at the surface, relatively quick diffusion of NaCl compared to solvent molecules and increased NaCl solubility due to depletion of the antisolvent (ethanol) for NaCl near the droplet surface enable the NaCl saturation ratio to be maximum at the droplet center. During evaporation, the droplet surface temperature increases quickly from the initial

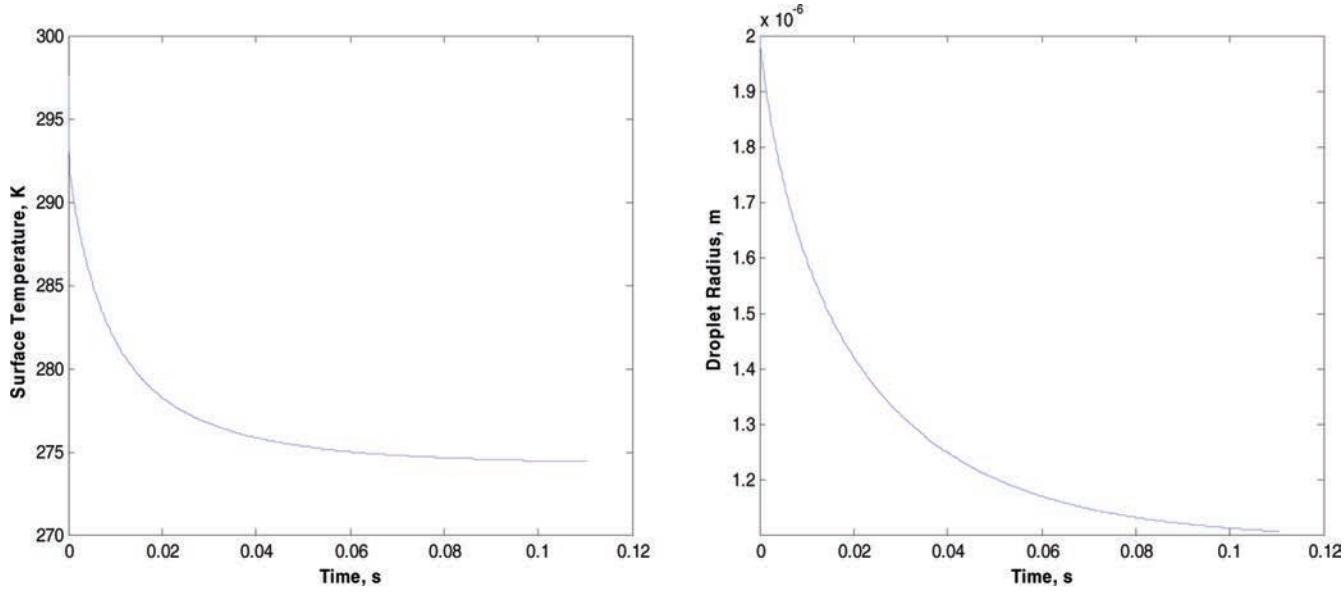

Figure 11. (a) 80% (v/v) droplet surface temperature change versus adiabatic evaporation time. (b) Droplet size change versus adiabatic evaporation time.

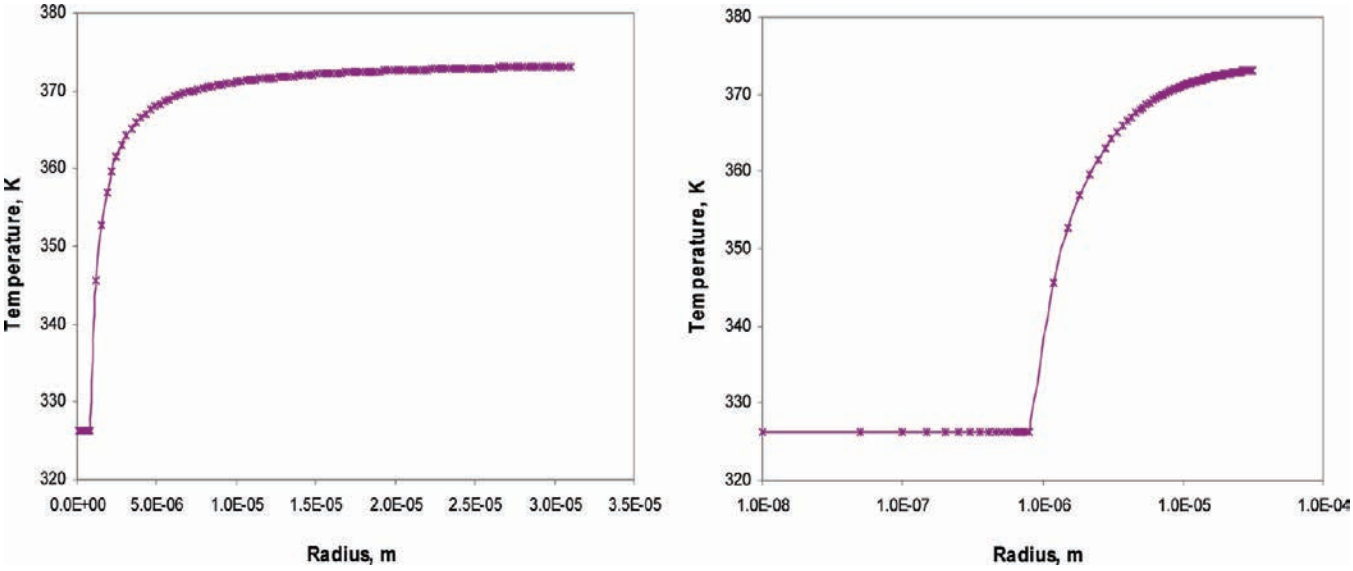

Figure 12. Temperature profile for the evaporation system after 0.183 ms of evaporation in N_2.

298.15 K to near 327 K, as shown in Figure 12. Figure 15 demonstrates evolution of the NaCl saturation ratio profile at the beginning of stable nucleus formation and after 28.7, 61.6, 96.3, and 131.6 μs of crystallization. Once nucleation and crystallization occur at the center, because the crystallization process is very quick and controlled by diffusion, the NaCl concentration is saturated at the crystal surface. This always keeps the saturation ratio at unity at the center and results in a sharp NaCl concentration gradient near the droplet center. Diffusion of NaCl to the center reduces the nearby NaCl concentration and decreases the saturation ratio. As evaporation proceeds, the droplet size decreases and the surface NaCl concentration keeps increasing after 28.7, 61.6, and 96.3 μs of crystallization. After 131.6 μs of crystallization, the saturation ratio reaches a maximum at the surface. The value is below the critical saturation ratio and continues to decrease with further evaporation, making it impossible to form additional stable nuclei in the droplet. The fast diffusion depletes NaCl in the droplet and quenches the formation of new nuclei, favoring one single crystal at the center. It takes only ~0.3 ms for the droplets from entering the heating zone to forming only a stable single crystal at the droplet center, corresponding to ~0.026 mm axial movement of aerosol droplets in the reactor tube. It is reasonable to select 100 °C as the representative heating temperature because the choice of a lower temperature, or treatment as a sequence of consecutive evaporation steps with increasing heating temperature, does not affect the conclusion. According to the simulation, if the droplet size and/or evaporation rate are sufficiently large, NaCl cannot diffuse quickly enough to the central nucleus to avoid exceeding the critical saturation in the droplet bulk, indicating that multiple NaCl nanocrystals will be formed in the final particles.

It should be pointed out that the initial droplet size, precursor composition, evaporation conditions, solubility, diffusion, vapor pressure, and heat transport all couple together in controlling the final particle morphology and structure. A combination of good solvent and antisolvent will favor the formation of only a single salt crystal or core inside each particle. Under aerosol generation and synthesis conditions, the droplet size is small and the growing assembled surfactant/silica layer provides a

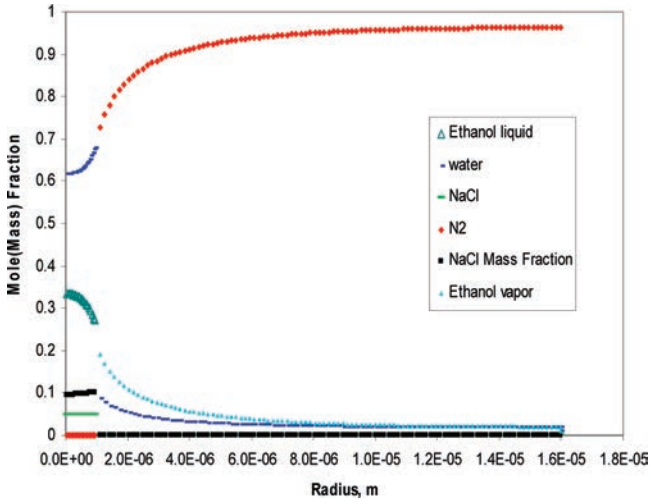

Figure 13. Mole fraction profiles for ethanol, water, NaCl, and N_2 in the droplet and vapor phase after 0.183 ms of evaporation in 100 °C nitrogen.

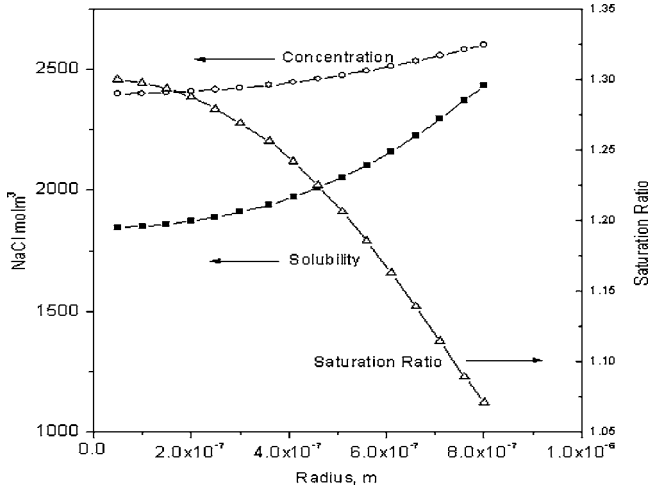

Figure 14. NaCl concentration, solubility, and saturation ratio after 0.183 ms of evaporation.

heat/mass-transfer barrier. The reduced evaporation rate and droplet surface temperature decrease the NaCl gradient. In addition, continuous formation of ethanol as a product of tetraethylorthosilicate hydrolysis sustains the ethanol concentration inside the droplet and maintains the ethanol gradient critical to the initial NaCl nucleation/crystallization at the center.

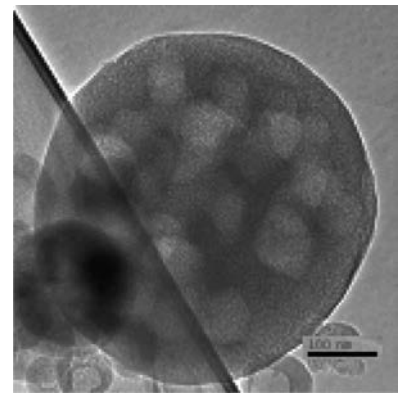

Figure 16. TEM image for a mesoporous silica particle with multiple embedded NaCl crystals fabricated with a ethanol-free precursor.

For a comparison, an ethanol-free precursor composed of 4.0 g of cetyltrimethylammonium bromide, 10.42 g of tetraethoxysilane (TEOS), 78.7 g of deionized water, and 1.10 g of 1 N HCl was used for aerosol-assisted EISA under the same conditions as those for Figure 8. Without the addition of ethanol, sol−gel reactions occur rapidly and less ordered silica particles with multiple NaCl crystals are formed (Figure 16). The delayed NaCl nucleation and crystallization and higher NaCl concentration favor the formation of multiple smaller NaCl crystals instead of a bigger single one.

Engineering of the Aerosol Particle Architecture. Inspired by the simulation, we fabricated aerosol particles of varying architectures. It is expected that high solvent evaporation temperatures lead to less dense particles and hollow particles, whereas low evaporation temperatures and initial concentrations near saturation favor the formation of dense solid particles.[19] Figure 17 shows hollow cerium oxide/chloride particles fabricated by the aerosol synthesis of $CeCl_3$−ethanol droplets at 400 °C.[14] We sprayed a metal oxide precursor in a hydrophobic low-boiling-point solvent (hexane) at room temperature.[34] Quick evaporation enriches the precursor concentration at the droplet surface, where hydrolysis and condensation of $CeCl_3$ results from the reaction with water supplied from the vapor phase. Because water diffusion is limited by the solubility of the hydrophobic solvent, this "sol gel" reaction occurs only at the droplet surface. In this way, we demonstrated a general facile

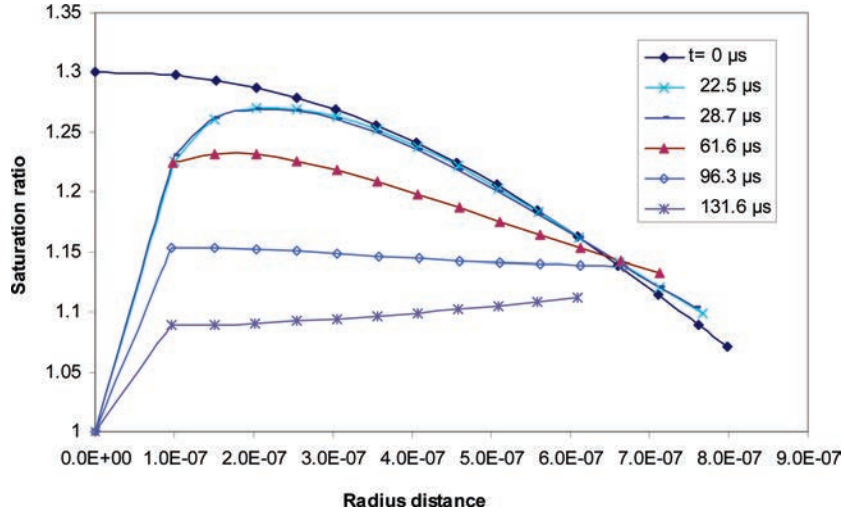

Figure 15. Effect of crystallization on the NaCl saturation ratio distribution.

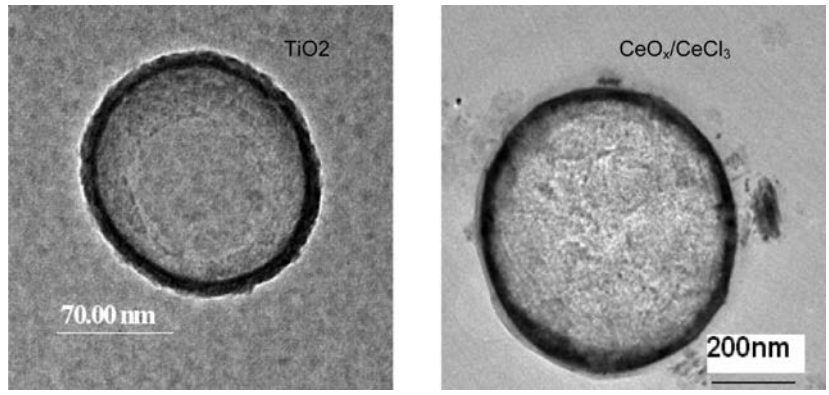

Figure 17. TEM images for hollow spherical particles: (left) Titania hollow particles made by spraying titanium tetraisopropoxide−hexane droplets at room temperature;[34] (right) Cerium oxide/chloride hollow particle made by spraying $CeCl_3$−ethanol droplets at 400 °C.

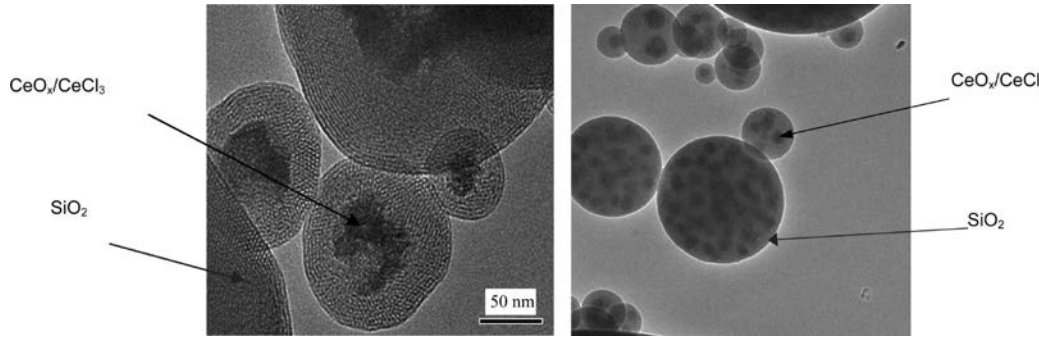

Figure 18. TEM images for cesium-containing silica particles. Core−shell ceria/cerium chloride/mesoporous silica particles prepared by aerosol processing of a water-based precursor (high solubility) at 400 °C (left). Silica nanoparticles containing multiple ceria/ceriachloride crystallites prepared by spraying an ethanol-based precursor (low solubility) at 400 °C (right).[14]

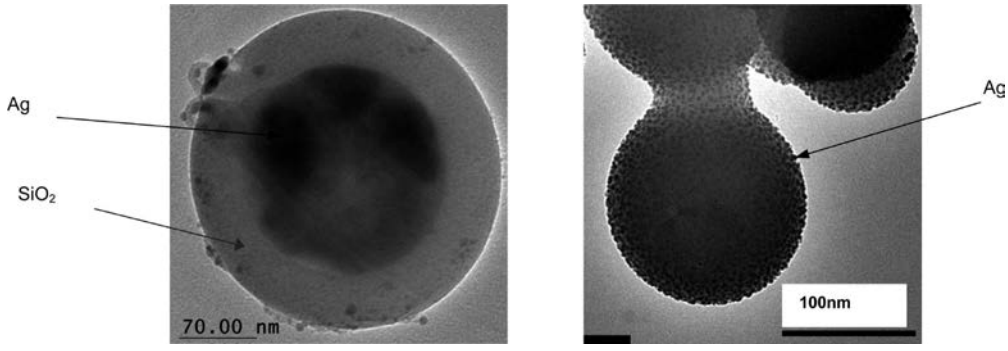

Figure 19. TEM images for silver/silica particles: (left) Single silver core−silica shell nanoparticle using TEOS as the silica precursor. (right) Multiple silver nanocluster@silica using (aminopropyl)triethoxysilane as both a silica precursor and a complexing agent for silver ions.[35]

room-temperature fabrication method[34] for hollow spherical metal oxide particles. The low-temperature technique works for encapsulation of heat-sensitive drug materials.[34] It is possible to fabricate hollow spherical particles at a low temperature even using a hydrophilic solvent if we increase the evaporation rate using a low-boiling solvent or operate under vacuum to suppress the droplet surface temperature and induce nucleation/crystallization to occur first at the droplet surface instead of the center.

It is found by the simulation that a lower salt solubility requires slower evaporation and/or a smaller droplet size to homogenize the salt concentration or else multiple stable nuclei and multicrystals will be formed. We have made single and multiple cerium compound cores in silica particles by selecting the solvents with varying solubility (Figure 18). In addition to the controls by solvent hydrophobicity, solubility, and evaporation rate, according to the simulation, if the salt ions have a high affinity for the gelling silica matrix, the much reduced diffusion coefficient of the ions will promote the formation of well-dispersed small uniform crystals in the matrix. Applying these principles, we also invented a technique[35] for antimicrobial agents in which silver nanoclusters are uniformly dispersed in silica particles (Figure 19).

Concluding Remarks

A simulation methodology/computer code has been developed for the study of the evaporation of multicomponent droplets. The code successfully describes water droplet and ethanol droplet evaporation and clearly demonstrates the accompanying evolution of composition, temperature, droplet size, and inhomogeneities. For ethanol−water−NaCl droplet evaporation, the aerosol mist can be assumed to be at equilibrium before entering the heating zone. After entering the heating zone, NaCl nucleation and crystallization occur quickly, starting first at the center. Crystallization depletes the surrounding region of NaCl, and only a single crystal is formed within each particle. The

code can be used to predict profiles for the temperature, size, and compositions for both pure and multicomponent evaporating droplets. So far, the temperature and concentration profiles within the droplets are difficult to study experimentally. The computer code provides sufficient accuracy for engineering design and provides a guideline for aerosol research such as evaporation-induced self-assembly and fabrication of nanostructured aerosol particles.

Appendix

Heat Capacity. The heat capacity for an ethanol (1)−water (2)−NaCl (3) solution is given as

$$C_p = C_p^E(X_1 + X_2) + X_1C_{P,1} + X_2C_{P,2} + X_3C_{P,3} \quad \text{(A-1)}$$

where the excess heat capacity excess C_{pm}^E was given by Benson and Darcy.[36]

Density. The density ρ (kg/m^3) for an ethanol−water−NaCl solution is given as[37]

$$\rho = 1000(A_0 + A_1w_1 + A_2w_2 + A_3w_1w_2 + A_4w_1w_2^2) \times \exp\left[A_5\left(\frac{w_2}{w_3}\right) + A_6\left(\frac{w_2}{w_3}\right)^2\right] \quad \text{(A-2)}$$

NaCl Solubility. In the temperature range 298−323 K, the solubility, S_{NaCl} (mol/kg), is given by Farelo et al.[38−40]

$$S_{NaCl} = \frac{0.0956424\exp(0.0072512T)(1 - X)}{0.0956424\exp(0.0072512T) + X}(7.78461 - 0.01566T + 0.000034T^2) \quad \text{(A-3)}$$

where X is the ethanol mass fraction in a salt-free solvent.

Diffusion Coefficients. The Vignes relationship[41] is used to determine binary diffusion coefficients at finite concentrations. The diffusion coefficients for ethanol and water can be assumed to be the same as those for a binary system, and the infinite diffusion coefficient for NaCl, D_{12}^0, can be estimated by the Wilke−Chang estimation[42,43]

$$D_{12}^0 = \frac{7.4 \times 10^{-8}(\phi M_2)^{1/2}T}{\eta_2 V_1^{0.6}} \quad \text{(A-4)}$$

For an ethanol−water solution, we replace the molecular weight term in eq A-4 with

$$\phi M = \sum x_i\phi_i \mathrm{MW}_i \quad \text{(A-5)}$$

For NaCl concentrations up to 2 M, the diffusion coefficient can be estimated by an empirical equation proposed by Gordon.[44]

$$D_{12} = D_{12}^0\frac{\eta_s}{\eta}(\rho_s\overline{V}_s)^{-1}\left(1 + m\frac{\partial \ln \gamma_\pm}{\partial m}\right) \approx D_{12}^0\left(1 + m\frac{\partial \ln \gamma_\pm}{\partial m}\right) \quad \text{(A-6)}$$

where m is the molarity of the solute (mol/kg of solvent), $\gamma_\pm$ the mean activity coefficient of the salt, ρ_s the molar density of the solvent, $\overline{V}_s$ the partial molar volume of the solvent, η_s the viscosity of the solvent, and η the viscosity of the solution.

Acknowledgment

T.L.W. was supported by NSF NIRT Grant EE C-0210835. X.J. performed all of the experimental work and was supported by the DOE NSET program DE-FG03-02ER15368. C.J.B. developed the aerosol-assisted EISA process and was supported by the DOE Office of Basic Energy Sciences Grant DE-FG02-02-ER15368 and SNL's Lab Directed Research and Development Program. Sandia is a multiprogram laboratory operated by Sandia Corporation, a wholly owned subsidiary of Lockheed Martin Company, for the United States Department of Energy's National Nuclear Security Administration under Contract DE-AC04-94AL85000.

Literature Cited

(1) Kammler, H. K.; Madler, L.; Pratsinis, S. E. Flame Synthesis of Nanoparticles. *Chem. Eng. Technol.* **2005**, *24* (6), 583–596.

(2) Pang, J. B.; Stuecker, J. N.; Jiang, Y. B.; Bhakta, A. J.; Branson, E. D.; Li, P.; Cesarano, J.; Sutton, D.; Calvert, P.; Brinker, C. J. Directed Aerosol Writing of Ordered Silica Nanostructures on Arbitrary Surfaces with Self-assembling Inks. *Small* **2008**, *4* (7), 982–989.

(3) Okuyama, K.; Lenggoro, I. W. Preparation of Nanoparticles via Spray Route. *Chem. Eng. Sci.* **2003**, *58* (3−6), 537–547.

(4) Lighty, J. S.; Veranth, J. M.; Sarofim, A. F. Combustion Aerosols: Factors Governing Their Size and Composition and Implications to Human Health. *J. Air Waste Manage.* **2000**, 1565–1618.

(5) Choy, K. L. Chemical Vapour Deposition of Coatings. *Prog. Mater. Sci.* **2003**, *48* (2), 57–170.

(6) Chan, H. K.; Clark, A.; Gonda, I.; Mumenthaler, M.; Hsu, C. Spray Dried Powders and Powder Blends of Recombinant Human Deoxyribonuclease (rhDNase) for Aerosol Delivery. *Pharm. Res.* **1997**, *14* (4), 431–437.

(7) Liu, J. W.; Jiang, X. M.; Ashley, C.; Brinker, C. J. Electrostatically Mediated Liposome Fusion and Lipid Exchange with a Nanoparticle-Supported Bilayer for Control of Surface Charge, Drug Containment, and Delivery. *J. Am. Chem. Soc.* **2009**, *131* (22), 7567.

(8) Liu, J. W.; Stace-Naughton, A.; Jiang, X. M.; Brinker, C. J. Porous Nanoparticle Supported Lipid Bilayers (Protocells) as Delivery Vehicles. *J. Am. Chem. Soc.* **2009**, *131* (4), 1354.

(9) Messing, G. L.; Zhang, S. C.; Jayanthi, G. V. Ceramic powder synthesis by spray-pyrolysis. *J. Am. Ceram. Soc.* **1993**, *76* (11), 2707–2726.

(10) Kodas, T. T.; Hamden -Smith, M. *Aerosol Processing of Materials*; Wiley-VCH: New York, 1999.

(11) Nasibulin, A. G.; Moisala, A.; Brown, D. P.; Jiang, H.; Kauppinen, E. I. A Novel Aerosol Method for Single Walled Carbon Nanotube Synthesis. *Chem. Phys. Lett.* **2005**, *402* (1−3), 227–232.

(12) Lu, Y. F.; Fan, H. Y.; Stump, A.; Ward, T. L.; Rieker, T.; Brinker, C. J. Aerosol-Assisted Self-Assembly of Mesostructured Spherical Nanoparticles. *Nature* **1999**, *398*, 223.

(13) Jiang, X. M.; Brinker, C. J. Aerosol-Assisted Self-Assembly of Single-Crystal Core/Nanoporous Shell Particles as Model Controlled Release Capsules. *J. Am. Chem. Soc.* **2006**, *128* (14), 4512–4513.

(14) Jiang, X. M. Engineering of Aerosol Nanoparticle Architectures. Ph.D. Dissertation, The University of New Mexico, Albuquerque, NM, 2006.

(15) Rathod, S. B.; Ward, T. L. Hierarchical Porous and Composite Particle Architectures Based on Self Assembly and Phase Separation in Droplets. *J. Mater. Chem.* **2007**, *17* (22), 2329–2335.

(16) Jiang, X. M.; Ward, T. L.; Cheng, Y. S.; Liu, J. W.; Brinker, C. J. Aerosol Fabrication of Hollow Mesoporous Silica Nanoparticles and Encapsulation of L-Methionine As A Candidate Drug Cargo. *Chem. Commun.* **2010**, *46*, 3019–3021.

(17) Eerikainen, H.; Watanabe, W.; Kauppinen, E. I.; Ahonen, P. P. Aerosol Flow Reactor Method for Synthesis of Drug Nanoparticles. *Eur. J. Pharm. Biopharm.* **2003**, *55* (3), 357–360.

(18) van der Lijn, J. *Simulation of Heat and Mass Transfer in Spray Drying*; Centre for Agricultural Publishing and Documentation: Wageningen, The Netherlands, 1976.

(19) Jayanthi, G. V.; Zhang, S. C.; Messing, G. L. Modeling of Solid Particle Formation During Solution Aerosol Thermolysis: The Evaporation Stage. *Aerosol Sci. Technol.* **1993**, *19*, 478–490.

(20) Asaithambi, N. S. A Variable Time Step Galerkin Method for A One-Dimensional Stefan Problem. *Appl. Math. Comput.* **1997**, *81* (2−3), 189–200.

(21) Caldwell, J.; Savovic, S.; Kwan, Y. Y. Nodal Integral and Finite Difference Solution of One-Dimensional Stefan Problem. *J. Heat Transfer* **2003**, *125* (3), 523–527.

(22) Moyano, E. A.; Scarpettini, A. F. Numerical Stability Study and Error Estimation for Two Implicit Schemes in a Moving Boundary Problem. *Numer. Methods, Part D and E* **2000**, *6* (1), 42–61.

(23) Homer, C. J.; Jiang, X. M.; Ward, T. L.; Brinker, C. J.; Reid, J. P. Measurements and simulations of the near-surface composition of evaporating ethanol−water droplets. *Phys. Chem. Chem. Phys.* **2009**, *11*, 7780–7791.

(24) Anderson, T. F.; Prausnitz, J. M. Application of The UNIQUA Equation to Calculation of Multicomponent Phase Equilibriua. 1. Vapor−Liquid Equilibria. *Ind. Eng. Chem. Process Des. Dev.* **1978**, *17* (4), 552–567.

(25) Iliuta, M. C.; Thomsen, K.; Rasmussen, P. Extended UNIQUAC Model for Correlation and Prediction of Vapour−Liquid−Solid Equilibria in Aqueous Salt Systems Containing Non-Electrolytes. Part A. Methanol−Water−Salt Systems. *Chem. Eng. Sci.* **2000**, *55* (14), 2673–2686.

(26) Thomsen, K.; Iliuta, M. C.; Rasmussen, P. Extended UNIQUAC Model for Correlation and Prediction of Vapor−Liquid−Liquid−Solid Equilibria in Aqueous Salt Systems Containing Non-Electrolytes. Part B. Alcohol (Ethanol, Propanols, Butanols)−Water−Salt Systems. *Chem. Eng. Sci.* **2004**, *59*, 3631–3647.

(27) Thomsen, K.; Rasmussen, P. Modeling of vapor−liquid−solid equilibrium in gas−aqueous electrolyte systems. *Chem. Eng. Sci.* **1999**, *54*, 1787–1802.

(28) Ranz, W. E.; Marshall, W. R., Jr. Evaporation from drops. *Chem. Eng. Prog., Part II* **1952**, *48* (4), 173.

(29) Hinds, W. C. *Aerosol Technology: Properties, Behavior, and Measurement of Airborne Particles*, 2nd ed.; Wiley-Interscience: New York, 1999.

(30) Sazhin, S. S. Advanced Models of Fuel Droplet Heating and Evaporation. *Prog. Energy Combust. Sci.* **2006**, *32* (2), 162–214.

(31) Devarakonda, V.; Ray, A. K. Determination of Thermodynamic Parameters from Evaporation of Binary Microdroplets of Volatile Constituents. *J. Colloid Interface Sci.* **2000**, *221* (1), 104–113.

(32) Devarakonda, V.; Ray, A. K. Effect of Inter-Particle Interactions on Evaporation of Droplets in A Linear Array. *J. Aerosol Sci.* **2003**, *34* (7), 837.

(33) Sangiovanni, J. J.; Labowsky, M. Burning Times of Linear Fuel Droplet Arrays—A Comparison of Experiment and Theory Combustion and Flame. *Combust. Flame* **1982**, *47* (1), 15.

(34) Jiang, X. M.; Brinker, C. J. Hollow Sphere Metal Oxides. U.S. Patent Application No. 0210,053, 2008.

(35) Jiang, X. M.; Brinker, C. J. Aerosol Method for Nano Silver−Silica Composite Anti-Microbial Agent. U.S. Patent Application No. 0175,948, 2009.

(36) Benson, G. C.; Darcy, P. J. Excess Isobaric Heat-Capacities of Water Normal-Alcohol Mixtures. *J. Chem. Eng. Data* **1982**, *27* (4), 439–442.

(37) Galleguillos, H. R.; Taboada, M. E.; Graber, T. A.; Bolado, S. Compositions, Densities, and Refractive Indices of Potassium Chloride Plus Ethanol Plus Water and Sodium Chloride Plus Ethanol Plus Water Solutions at (298.15 and 313.15) K. *J. Chem. Eng. Data* **2003**, *48* (2), 405–410.

(38) Farelo, F.; Lopes, A. M. C.; Ferra, M. I. Solubities of Sodium Chloride and Potassium Chloride in Water + Ethanol Mixtures from (298 to 323) K. *J. Chem. Eng. Data* **2004**, *49* (6), 1782–1788.

(39) Pinho, S. P.; Macedo, E. A. Solubility of NaCl, NaBr, and KCI in Water, Methanol, Ethanol, and Their Mixed Solvents. *J. Chem. Eng. Data* **2005**, *50* (1), 29–32.

(40) Nicolaisen, H.; Rasmussen, P.; Sørensen, J. M. Correlation and Prediction of Mineral Solubilities in the Reciprocal Salt System (Na^+, K^+)(Cl^-, $SO4^{2-}$)−H_2O at 0−100 °C. *Chem. Eng. Sci.* **1993**, *48* (18), 3149–3158.

(41) Vignes, A. Diffusion in Binary Solutions. *Ind. Eng. Chem. Fundam.* **1966**, *5* (2), 189.

(42) Perry, R. H., Green, D. W., Maloney, J. O., Eds. *Perry's Chemical Engineers' Handbook*, 6th ed.; McGraw-Hill: New York, 1997.

(43) Lide, D. R., Ed. *Handbook of Chemistry and Physics*, 73rd ed.; CRC Press: Boca Raton, FL, 1992.

(44) Gordon, A. R. The Diffusion Constant of An Electrolyte, and Its Relation to Concentration. *J. Chem. Phys.* **1937**, *5*, 522–526.

Received for review December 23, 2009
Revised manuscript received April 28, 2010
Accepted May 5, 2010

IE902042Z